

Models for Type Ia Supernovae and Cosmology

Peter Höflich

Department of Astronomy, University of Texas, Austin, TX 78681, USA

Abstract. From the spectra and light curves it is clear that SNIa events are thermonuclear explosions of white dwarfs. However, details of the explosion are highly under debate. Here, we present detailed models which are consistent with respect to the explosion mechanism, the optical and infrared light curves (LC), and the spectral evolution. This leaves the description of the burning front and the structure of the white dwarf as the only free parameters. The explosions are calculated using one-dimensional Lagrangian codes including nuclear networks. Subsequently, optical and IR-LCs are constructed. Detailed NLTE-spectra are computed for several instants of time using the density, chemical and luminosity structure resulting from the LCs (sect.2).

Different models for the thermonuclear explosion are discussed including detonations, deflagrations, delayed detonations, pulsating delayed detonations (PDD) and helium detonations (sect.3). Comparisons between theoretical and observed LCs and spectra provide an insight into details of the explosion and nature of the progenitor stars (sect. 4 & 5). We try to answer several related questions. Are subluminescent SNe Ia a group different from ‘normal’ SN Ia (sect. 4)? Can we understand observed properties of the LCs and spectra (sect. 5)? What can we learn from infrared spectra? Can we determine H_o independently from primary distance indicators, and how do the results compare with empirical methods (sect.6)? What do we learn about the progenitor evolution and its metallicity? What are the systematic effects for the determination of the cosmological parameters Ω_M and Λ and how can we recognize this potential ‘pitfalls’ and correct for evolutionary effects (sect.7)?

1. Introduction

During the last few years it became evident that Type Ia supernovae are a less homogeneous class than previously believed (e.g. Barbon et al., 1990, Pskovskii 1970, Phillips et al. 1987). In particular, the observation of subluminescent SN1991bg (Fillipenko et al. 1992, Leibundgut et al. 1993) raised questions on the SN-rate and whether we have missed a huge subgroup. The possible impact on our understanding of supernovae statistics and, consequently, the chemical evolution of galaxies must be noted.

With respect to the use of Type Ia Supernovae as distance indicators, for nearby supernovae ($z \leq 0.1$), different schemes have been developed and tested to cope with the problems of deducing the intrinsic brightness based on theo-

retical models or observed correlations between spectra or light curves and the absolute brightness using primary distance indicators (e.g. Norgaard-Nielsen et al. 1989; Branch & Tammann 1992, Sandage & Tammann 1993, Müller & Höflich 1994, Hamuy et al. 1996; Ries, Kirshner & Press 1995; Höflich & Khokhlov 1996, HK97 thereafter). These methods have been tested locally and provide consistent results. Due to the new recalibrations of the brightness of SNe Ia by δ Cephei in nearby galaxies (e.g. Saha et al. 1997 and references therein), a common agreement could be reached on the value of H_0 . In a next step, new telescopes and observational programs put SNe Ia at large red shifts well within reach and justify optimism for the discovery of a large number of distant SNe Ia. The Berkeley group has discovered more than 50 SNe Ia up to a red shift of 0.9 (Pennypacker et al. 1991, Perlmutter et al. 1997; Pennypacker, private communication). The CfA/CTIO/ESO/MSSSO collaboration has found a similar number of supernovae (Leibundgut et al. 1995, Schmidt et al. 1996). A major concern with the use of SNe Ia to determine q_0 is systematic errors due to evolutionary effects (Höflich et al. 1997). This is especially true for statistical methods which are calibrated only on local SNe Ia.

Despite the success of purely empirical methods, theoretical work on SNe Ia is critical to provide an independent test for the distance scale, to get an insight into the underlying physics of the explosion, it provides a tool to investigate benefits of new wavelength ranges not yet well explored (i.e. the IR) and it allows to test for the importance (or unimportance) of systematic effects when it comes to the study of very distant SNe Ia. The goal of this paper is to provide a brief overview of the different aspects just mentioned.

2. Numerical Methods

A consistent treatment of the explosion, light curves and spectra is critical to provide a tight coupling between the explosion model and the observational quantities. Therefore, we start with a brief description of the numerical methods.

2.1. Hydrodynamics

The explosions are calculated using a one-dimensional radiation-hydro code, including nuclear networks (HK96 and references therein). This code solves the hydrodynamical equations explicitly by the piecewise parabolic method (Collela & Woodward 1984) and includes the solution of the frequency averaged radiation transport implicitly via moment equations, expansion opacities, and a detailed equation of state. The frequency averaged variable Eddington factors and mean opacities are calculated by solving the frequency dependent transport equations. About one thousand frequencies (in one hundred frequency groups) and about five hundred depth points are used. Nuclear burning is taken into account using a network which has been tested in many explosive environments (see Thielemann, Nomoto & Hashimoto 1996 and references therein).

2.2. Light Curves

Based on the explosion models, the subsequent expansion and bolometric as well as monochromatic LCs are calculated using a scheme recently developed, tested

and widely applied to SN Ia (e.g. Höflich et al. 1993, Höflich et al. 1997ab and references therein). The code used in this phase is similar to that described above, but nuclear burning is neglected and γ ray transport is included via a Monte Carlo scheme (Höflich, Müller & Khokhlov 1992). In order to allow for a more consistent treatment of scattering, we solve both the (two lowest) time-dependent radiation moment equations for the radiation energy and the radiation flux, and a total energy equation. At each time step, we then use $T(r)$ to determine the Eddington factors and mean free paths of photons by solving the frequency-dependent radiation transport equation in comoving frame (see next section) in about 100 frequency bands (see below) and integrate to obtain the frequency-averaged quantities. We use the latter to iterate the solution with the frequency-integrated energy and flux equations. The frequency averaged opacities, have been calculated under the assumption of local thermodynamical equilibrium. This is a reasonable approximation for the light curve since diffusion time scales are always governed by layers of large optical depths. Note that the comparison of $L(r)$ between the frequency independent solution and the frequency dependent solution provides a critical test for the consistency of the approximations used in the radiation hydro.

Both the monochromatic and mean opacities are calculated using the Sobolev approximation (Sobolev 1957) to calculate the absorption probability within a shell and to include line blanketing. The approach is similar to Karp et al. (1977) but generalized for the comoving frame and the integration boundaries are adjusted to a radial grid (Höflich 1990). The scattering, photon redistribution and thermalization terms used in the light curve opacity calculation are calibrated with NLTE calculations using the formalism of the equivalent-two-level approach (Höflich 1995).

To calculate the monochromatic light curves, we use the $T(r)$ with the time dependence of the structure given by the frequency-integrated solution of the momentum equations to solve the frequency-dependent transfer equations in LTE every 0.2 to 0.5 days solution to get L_ν in the observer's frame. The broad band light curves are determine by convolution of L_ν with the filter functions. We use a few hundred frequency bands with the same scheme as described in the following subsection. Note that a proper treatment of the frequency derivatives in the comoving frame equations requires the use of about 5 to 10 times more frequencies than frequency bands. To test the consistency between the frequency-dependent and frequency-independent calculations we also integrate the L_ν and check to see how close the resulting L is to that from the solution of the frequency-integrated moment equations. The solutions are consistent within 10 % (see e.g. Khokhlov et al. 1993, Höflich et al. 1997b). Monochromatic colors from our light curve code have been compared to colors calculated by our detailed NLTE spectral code (Höflich 1995). Based on this comparison, the solutions for the Type Ia models are good to better than 0.1 mag near maximum light and deteriorate to 0.3 mag at about 100 days. Note that these tests probe the internal consistency only. However, a direct comparison of the bolometric correction of observed supernovae and of the theoretical models provide an independent test for systematic errors and, in particular, for the (critical) translation of bolometric into monochromatic brightness. For the well observed supernovae SN 1992a, accurate BCs have been reconstructed and found to be

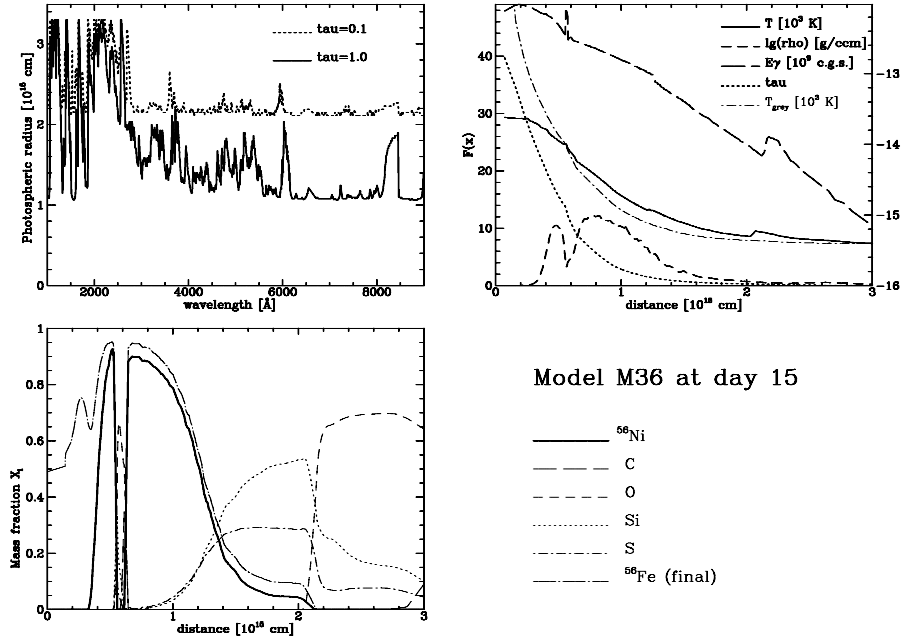


Figure 1. Various quantities for M36 15 days after the explosion. Distances are given as a function of wavelength at which the monochromatic optical depth reaches 0.1 and 1, respectively (upper left), Temperature T , density ρ , energy deposition due to radioactive decay E_γ and Rosseland optical depth are given as a function of distance and, for comparison, T_{grey} for the grey extended atmosphere (upper right), and chemical profile are presented for the most abundant elements (lower).

consistent with our models within 0.1^m (HK96). According to the certainties, uncertainties in the rise times are about 1-2 days due to the flat maxima.

2.3. NLTE-Spectra

Finally, detailed NLTE spectra have been constructed based on the LC calculations. Thus, the effect of energy stored during previous epochs is properly taken into account. The energetics of the model are calculated. Given an explosion model, the evolution of the spectrum is not subject to any tuning or free parameters such as the total luminosity. A modified version of our code for Nlte Extended ATmospheres (NEAT) is used. Although time dependence in the rate equations can be included in this code, it was found to be For details see Höflich (1990, 1995), Höflich et al. (1997b) and references therein.

For the NLTE spectra, the density, chemical profiles and the luminosity as a function of the radial distance r are given by the hydrodynamical explosion and the LC calculations, including the Monte-Carlo scheme for γ -ray transport.

The radiation transport equation is solved in the comoving frame including relativistic terms. For the determination of the first moment of the intensity, we solve the radiation transport equation for strong lines including ‘quasi’ continua (weak lines are treated in a Solovév approximation, see below) in the comoving

frame, i.e.

$$Op I = \chi(S - I)$$

$$I = I(\mu, r, \nu); \quad S = S(r, \nu); \quad \chi = \chi(r, \nu)$$

(μ : cosine between the radial direction and I; r : radial distance; $v(r)$: radial velocity; S : source function; χ : absorption coefficient; ν : frequency). The operator Op can be written as follows (Castor, 1974):

$$Op = \left[\mu + \frac{v(r)}{c} \right] \frac{\partial}{\partial r} + \left[\frac{(1 - \mu^2)}{r} \left(1 + \frac{\mu v(r)}{c} (1 - \beta(r)) \right) \right] \frac{\partial}{\partial \mu} - \left[\frac{v(r)\nu}{c \cdot r} (1 - \mu^2 + \mu^2 \beta(r)) \right] \frac{\partial}{\partial \nu} + \left[\frac{3v(r)}{c \cdot r} (1 - \mu^2 + \beta(r)\mu^2) \right]$$

with

$$\beta := \frac{d \ln v(r)}{d \ln r}.$$

The term in front of $\frac{\partial}{\partial \nu}$ can be interpreted as the classical Doppler shift. The second terms of the partial derivatives with respect to r , μ and the logarithmic derivative of $v(r)$ correspond to the advection and aberration effects. For practical purpose, we solve the non relativistic transport equation using a Rybicki scheme (Mihalas et al., 1975, 1976ab). Overlapping lines in the comoving frame cannot be treated because the system is solved as a boundary problem in the frequency space which, from the concept, disallows a propagation of information toward higher/lower frequencies for expanding/collapsing envelopes. The same limitation should also apply to Nugent et al. (1995a) who use the same method. However, the problem of overlapping lines can be and has been solved (Höflich 1990) in full analogy with the problem of partial redistribution using a Fourrier-like scheme (Mihalas et al, 1976b). Although our code can deal with partial redistribution, this effect is neglected to save CPU-time. A technical problem is the fact that each line must be sampled by at least 10 frequency points to provide a sufficient accurate representation of the $\delta/\delta\nu$ -term (Mihalas et al. 1975). Currently, we must limit this approach to $\approx 10,000$ lines.

Blocking by lines other than the strong ones is included in a ‘quasi’ continuum approximation, i.e. the frequency derivative terms in the radiation transport equation is included in the narrow line limit to calculate the probability for photons to pass a radial sub-shell along a given direction μ (Castor, 1974, Abbot and Lucy 1985, Höflich, 1990). Note that the information on the exact location of the interaction within a subshell gets lost translating into an uncertainty in the wavelength location of $\approx 10^{-3}$.

The statistical equations are solved consistently with the radiation transport equation to determine the non-LTE occupation numbers using both an accelerated lambda iteration (see Olson et al. 1986) and an equivalent-two level approach for transitions from the ground state which provides an efficient way to take the non-thermal fraction of the source function into account during the radiation transport and, effectively, accelerate both the convergence rate and the stability of the system. A comparison of the explicit with the implicit source functions provides a sensitive tool to test for convergence of the system of rate and radiation transport equations.

Excitation by gamma rays is included. Detailed atomic models are used for up to three most abundant ionization stages of several elements, i.e. (He), C, O, Ne, Na, Mg, Si, S, Ca, Fe taking into account 20 to 30 levels in the main ionization stage. Currently, we use detailed term-schemes for C, O, Ne, Na, Mg, Si, S, Ca, Fe, Co and Ni. The corresponding lower and upper ions are represented by the ground states. The energy levels and cross sections of bound-bound transitions are taken from Kurucz (1993). A total of 10,000 lines are treated in full NLTE. In addition, $\approx 1,000,000$ lines out of a list of 31,000,000 (Kurucz, 1993) are included for the radiation transport. For these lines, we assume LTE population numbers inside each ion. To calculate the ionization balance, excitation by hard radiation is taken into account. LTE-line scattering is included using an equivalent-two-level approach calibrated by our NLTE-elements.

The need for spectral analyses consistent with respect to the explosion mechanism, γ -ray transport and LC calculation is obvious from Fig. 1 No well defined photosphere exists. Already at maximum light, the chemical distribution of elements does not follow the density profile but shows large individual variations in the line forming region, i.e. between 1 and $2 \cdot 10^{15}$ cm. The energy deposition and excitation due to γ -rays becomes important within the photosphere. Consequently, the luminosity cannot be assumed to be depth independent for the construction of synthetic spectra.

3. Hydrodynamical Models

3.1. Explosions of Massive White Dwarfs

A first group consists of massive carbon-oxygen white dwarfs (WDs) with a mass close to the Chandrasekhar mass which accrete mass through Roche-lobe overflow from an evolved companion star (Nomoto & Sugimoto 1977). The explosion is triggered by compressional heating. The key question is how the flame propagates through the white dwarf. Several models of SNeIa have been proposed in the past, including detonation (Arnett 1969; Hansen & Wheeler 1969), deflagration (e.g. Nomoto, Sugimoto & Neo 1976) and the delayed detonation model, which assumes that the flame starts as a deflagration and turns into a detonation later on (e.g. Khokhlov 1991ab, Woosley & Weaver 1994).

Our sample includes detonations (DET1/2), deflagrations (W7, DF1), delayed detonations (M35-39, DD13-27, DD200) and pulsating delayed detonations (PDD1-9). The deflagration speed is parameterized as $D_{def} = \alpha a_s$, where a_s is the local sound velocity ahead of the flame and α is a free parameter. The speed of the detonation wave is given by the sound-speed behind the front. For delayed detonation models, the transition to a detonation is given by another free parameter ρ_{tr} . When the density ahead of the deflagration front reaches ρ_{tr} , the transition to a detonation is forced by increasing α to 0.5 over 5 time steps bringing the speed well above the Chapman-Jouguet threshold for steady deflagration. For pulsating delayed detonation models, the initial phase of burning fails to release sufficient energy to disrupt the WD. During the subsequent contraction phase, compression of the mixed layer of products of burning and C/O formed at the dead deflagration front would give rise to a detonation via compression and spontaneous ignition (Khokhlov 1991ab). In this scenario, ρ_{tr} represents the density at which the detonation is initiated after the burning front

Table 1. Some quantities are given for our models (see text).

Model	M_* [M_\odot]	ρ_c [$10^9 c.g.s$]	α	ρ_{tr} [$10^7 c.g.s$]	M_{Ni} [M_\odot]
DET1	1.4	3.5	—	—	0.92
DF1	1.4	3.5	0.30	—	0.50
W7	1.4	2.0	n.a.	—	0.59
M35	1.4	2.8	0.03	3.0	0.67
M36	1.4	2.8	0.03	2.4	0.60
M37	1.4	2.8	0.03	2.0	0.51
M39	1.4	2.8	0.03	1.4	0.34
DD200c	1.4	2.0	0.03	2.0	0.61
DD13c (1:1)	2.6	0.03	3.0	1.36	0.79
DD21c (1:1)	1.4	2.6	0.03	2.7	0.69
DD23c (2:3)	1.4	2.6	0.03	2.7	0.59
PDD3	1.4	2.1	0.04	2.0	0.49
PDD5	1.4	2.7	0.03	0.76	0.12
PDD8	1.4	2.7	0.03	0.85	0.18
PDD7	1.4	2.7	0.03	1.1	0.36
PDD9	1.4	2.7	0.03	1.7	0.66
PDD6	1.4	2.7	0.03	2.2	0.56
PDD1a	1.4	2.4	0.03	2.3	0.61
PDD1c	1.4	2.4	0.03	0.71	0.10
HeD2	0.6+0.22	.013	—	—	0.43
HeD4	1.0+0.18	.150	—	—	1.07
HeD6	0.6+0.172	.0091	—	—	0.252
HeD10	0.8+0.22	.036	—	—	0.75
HeD12	0.9+0.22	.083	—	—	0.92
DET2	1.2	0.04	—	—	0.63
DET2env2	1.2 + 0.2	0.04	—	—	0.63
DET2env4	1.2 + 0.4	0.04	—	—	0.63

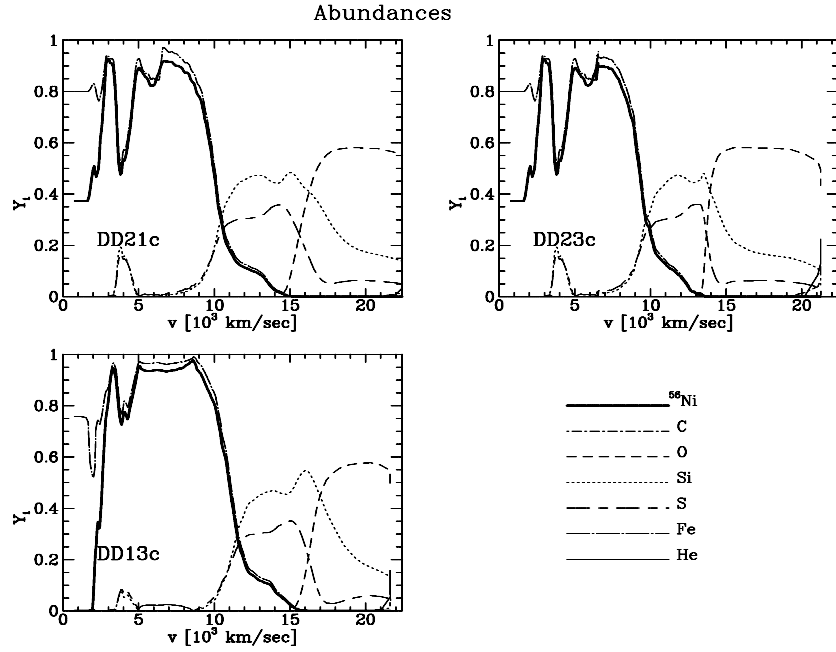


Figure 2. Abundances as a function of the expansion velocity for three delayed detonation models (see Table 1).

dies out. Besides the description of the burning front, the central density of the WD at the time of the explosion is another free parameter. For white dwarfs close to the Chandrasekhar limit, it depends sensitively on the chemistry and the accretion rate \dot{M} at the time of the explosion.

In addition, the C/O ratio has been varied. In general, it has been assumed to be 1:1 unless otherwise quoted in brackets after the name. A lower C/O ratio can be expected if the WD originates from a progenitor of more than $\approx 3M_{\odot}$. The initial metallicity for $Z \geq 20$ is assumed to be solar, but for DD24c, DD25c, DD26c and DD27c for which 1/3, 3, 0.1 and 10 times solar abundances are used, respectively. Otherwise, these models are identical to DD21c.

As example, typical chemical structures are given in Fig. 2. Since the burning time scales to NSE or partial NSE are shorter than the hydrodynamical time scales for all but the very outer layers, the final products depend mainly on the density at which burning takes place. With decreasing transition density, lesser ^{56}Ni is produced and the intermediate mass elements expand at lower velocities because the later transition to a detonation allows for a longer pre-expansion of the outer layers (DD21c vs. DD13c). Similarly, with increasing C/O ratio in the progenitor, the specific energy release during the nuclear burning is reduced (DD23c vs. DD21c) and the transition density at the burning front reached later in time, resulting in a larger preexpansion of the outer layers. This may allow to determine the main sequence mass of the progenitor.

To test the influence of the metallicity (i.e. nuclei beyond Ca) we have constructed models with parameters identical to DD21c but initial metallicities between 0.1 and 10 times solar. The energy release, the density and velocity structure are virtually identical to that of DD21c. The main difference is an increase of more neutron-rich Fe group nuclei, namely ^{54}Fe , in the outer layers because, there, Y_e is inherited from the progenitor. While, for 1/3 solar metallicity, hardly any ^{54}Fe is produced at high velocities, ^{54}Fe is as high as 5 % by mass fraction if we start with ten times the solar metallicity (see sect. 7). Note that the temperature in the inner layers is sufficiently high during the explosion to allow electron capture which determines Y_e and, in those layers, the initial metallicity has no influence on the final burning product (Höflich et al. 1997b).

3.2. Merging White Dwarfs

The second group of progenitor models consists of two low-mass white dwarfs in a close orbit which decays due to the emission of gravitational radiation and this, eventually, leads to the merging of the two WDs (e.g. Iben & Tutukov 1984). After the initial merging process, one low density WD is surrounded by an extended envelope (Hachisu, Eriguchi & Nomoto 1986, Benz, Thielemann & Hills 1989). This scenario is mimicked by our envelope models DET2env2...6 in which we consider the detonation in a low mass WD surrounded by a compact envelope between 0.2 and 0.6 M_{\odot} .

3.3. Explosions of Sub-Chandrasekhar Mass White Dwarfs

Another class of models – double detonation of a C/O-WD triggered by detonation of helium layer in low-mass WDs – was explored by Nomoto (1980), Woosley & Weaver (1980), and most recently by Woosley and Weaver (1994,

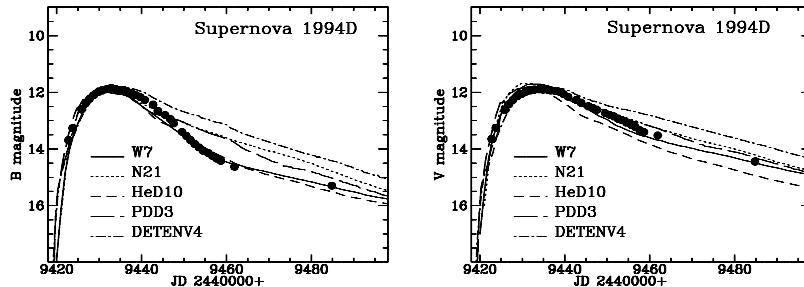


Figure 3. Theoretical LCs of the deflagration W7, the delayed detonation N21, the helium detonation HeD10, the pulsating delayed detonation PDD3, and the envelope model DET2env4. For comparison, the observation for SN1994D are given.

hereafter WW94), Livne & Arnett (1995) and HK96. For these models, the mass of the C/O core and of the He-layers given separately.

For ease of comparison, we have used parameters close to those suggested in WW94. To prevent repetition, we refer to the latter work for a detailed discussion of this class of models. Helium detonations show a qualitatively different structure in comparison to all models with a Chandrasekhar mass WD. The intermediate mass elements are sandwiched by Ni and He/Ni rich layers at the inner and outer regions, respectively. Generally, the density smoothly decreases with mass because partial burning produces almost the same amount of kinetic energy as the total burning, but a moderate shell-like structure is formed just below the former Helium layers. Observationally, a distinguishing feature of this scenario is the presence of Helium and Ni with expansion velocities above 11,000 to 14,000 $km s^{-1}$. Typically 0.07 to 0.13 M_{\odot} of Ni are produced in the outer layers, mainly depending on the mass of the Helium shell.

4. General Properties of the Explosion Models

The different explosion scenarios can generally be distinguished based on differences in the slopes of the early monochromatic LCs (Fig. 3 and spectra (Fig. 4), e.g. by the expansion velocities indicated by various elements. Note that the differences between the slopes of the LCs are much larger than the uncertainties imposed by the model assumptions (see sect. 2).

For all models with a ^{56}Ni production $\geq 0.4M_{\odot}$, M_V ranges from -19.1 to -19.7 m (HK96). As a general tendency, the post-maximum declines are related to M_V , but there is a significant spread in the decline rate among models with similar brightness. For all models but the Helium detonations, the colors become very red for small M_{Ni} consistent with the observations (Hamuy et al. 1996; Höflich et al. 1996).

The maxima of subluminal supernovae are more pronounced. For bright models, the opacity stays high and the photosphere recedes mainly by the geometrical dilution of matter. For models with a slower rise time or little ^{56}Ni , the opacity drops strongly at about maximum light. The photosphere recedes quickly in mass, and thermal energy can be released from a larger region. Be-

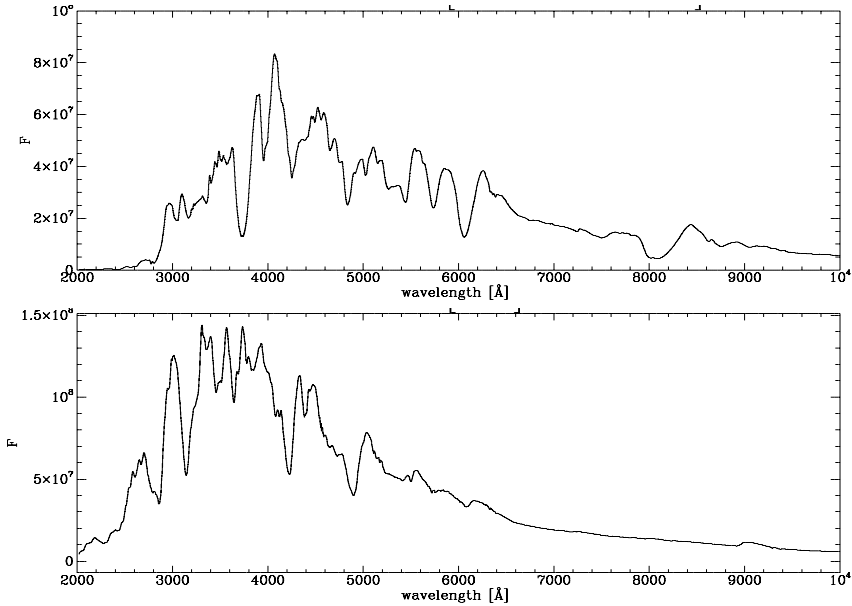


Figure 4. Comparison of spectra at about maximum light of the typical delayed detonation model DD200 and the normal bright helium detonation model HeD10 (lower graph).

cause no additional energy is gained, the energy reservoir is exhausted faster, and the post-maximum decline becomes steeper.

The blue and UV spectrum of the delayed detonation model is dominated by strongly blended lines due to Fe group elements. Strong features due to Si II at $\approx 6100\text{\AA}$ and Ca II at about $\approx 3800\text{\AA}$ and 8100\AA are consistent with observations. In contrast, the spectra of Helium detonations are very blue due to the heating by radioactive Ni both for normal and subluminous SNe Ia and the spectra are dominated by strong Ni lines without showing a strong Si line. Already from the general properties, these HeDs can be ruled out as a general scenario.

5. Comparison between Observation and Models Predictions

To get more information, detailed fitting of individual supernovae is required. The following 29 SNe Ia have been analysed: SN 37C, SN 70J, SN 71G, SN 72E, SN 72J, SN 73N, SN 74G, SN 75N, SN 81B, SN 83G, SN 84A, SN 86G, SN 88U, SN 89B, SN 90N, SN 90T, SN 90Y, SN 90af, SN 91M, SN 91T, SN 91bg, SN 92G, SN 92K, SN 92bc, SN 92bo, SN 94D, SN 94M, SN 94S, SN 94T (HK96, Höflich et al. 1997a, and references therein). For an example, see Figs. 5 6 7. To fit the light curves, we use a quantitative method for fitting data to models based on Wiener filtering (Rybicki and Press, 1995). The reconstruction technique is applied to the standard deviation from the theoretical LC to avoid problems with measurements distributed unevenly in time. By minimizing the error, the time of the explosion, the distance, and the reddening correction can be determined.

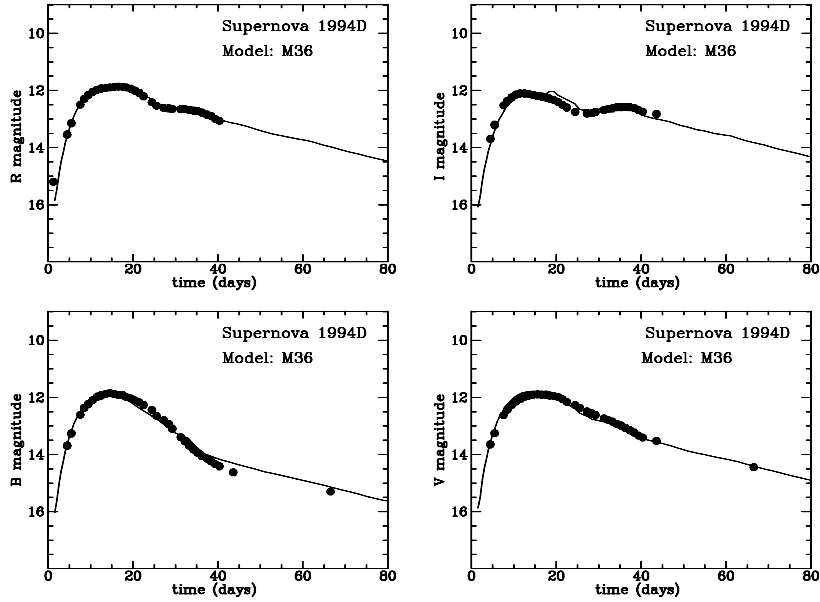


Figure 5. Observed LCs of SN 1994D in comparison with the theoretical LCs of M36

According to our results, normal bright, fast SNeIa (e.g. SN 71G, SN 94D) with rise times up to 18 days for the visual LC can be explained by delayed detonation with different densities ρ_{tr} for the transition from a deflagration to a detonation. For PDDs, the density ρ_{tr} stands for the density at which the detonation starts after the first pulsation. Typically, ρ_{tr} is about $2.5 \cdot 10^7 \text{ g cm}^{-3}$. Central densities of the initial WDs range from 2.1 to $3.5 \cdot 10^9 \text{ g cm}^{-3}$. As a tendency, models at the lower end of this range give better fits. We note that the classical deflagration W7 (Nomoto et al. 1984) provides similar good fits in several cases because its structure resembles those of DD models but it has some problems with the high velocities of Si lines in SN1994D (Höflich 1995).

The “standard” explosion models are unable, however, to reproduce very slow rise times (≥ 18 -20 days) even within the uncertainties, unless the C/O ratio is rather low (see sect. 7, Höflich et al. 1997b), or by models with an envelope of typically 0.2 to $0.4 M_{\odot}$. The envelope can be produced during a strong pulsation or during the merging of two WD. Distinguishing features between the alternatives of low C/O ratio and an envelope is the presence of unburned material and the absence of high velocity Si in the latter case, and a slow decline rate compared to DDs (see also sect. 7). Another, unique features of models with massive envelopes are very high photospheric expansion velocities ($v_{ph} \approx 16,000 \text{ km/s}$) shortly before maximum light, which drop rapidly to an almost constant value between 9000 and $12,000 \text{ km/s}$. This “plateau” in v_{ph} lasts for 1 to 2 weeks depending on the envelope mass (Khokhlov et al. 1993). In fact, there is some evidence for the plateau in v_{ph} from the Doppler shift of lines for SNe Ia with a slow pre-maximum rise and post-maximum decline (e.g. SN 84A, SN 90N, Müller & Höflich 1994) and, for SN1991T, there is evidence of unburned carbon down to velocities of $16,000 \text{ km/sec}$ (Branch, this volume).

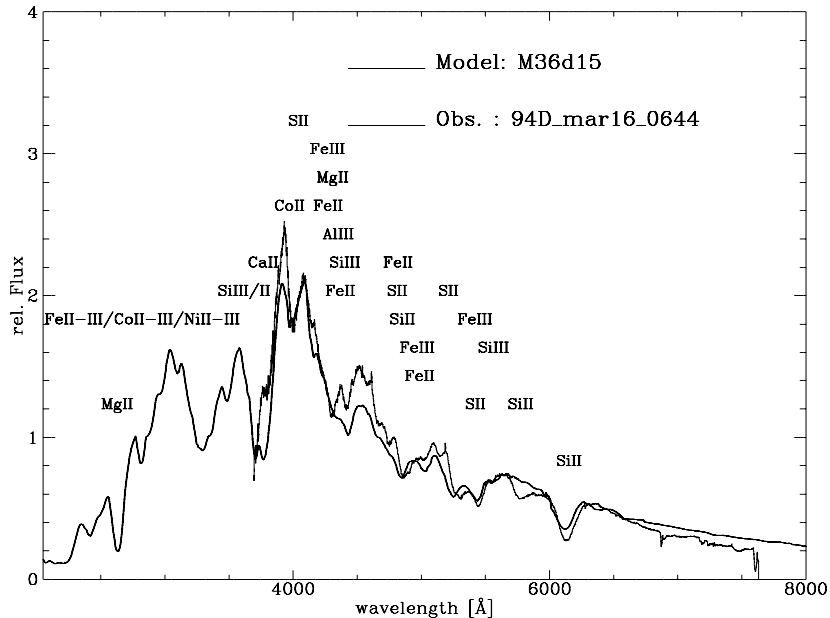


Figure 6. Synthetic spectrum at day 15 for M36 compared to the observations of SN1994D at Mar. 16th.

Qualitatively, strongly subluminous SNe Ia (SN 91bg, SN 92K, SN 92bc) can be explained within the framework of pulsating delayed detonation models with a low transition density which produce a very low mass envelope and very little ^{56}Ni but Si down to small expansion velocities (Höflich et al. 1995). Due to the small heating, these models become systematically redder and the post-maximum decline becomes steeper with decreasing brightness in agreement with observations. The evolution of the photospheric expansion velocity v_{ph} and, in particular, its steady decline, is consistent with observations. Note that some of the ‘classical’ delayed detonation models (M39) also produce strongly subluminous LCs, but these do not fit any of the measurements.

5.1. IR-Spectra

Despite very interesting results from the IR, spectroscopic analysis of early time infrared spectra of supernovae in the literature is limited and focused on individual features. E.g. Meikle et al. (1996) concentrated on determining the origin of a feature at $1.05\text{-}\mu\text{m}$ in the spectra of SN 1994D. They concluded that the feature might be due to either HeI $1.083\ \mu\text{m}$ or MgII $1.0926\ \mu\text{m}$, but found difficulties with both identifications. Graham (1986) attributed the $1.2\text{-}\mu\text{m}$ spectroscopic feature to absorption by a multiplet of SiI. Spyromilio et al. (1994) argued that no multiplet or combination of lines is responsible for the lack of flux in this spectral region. Instead, it is the absence of a line blanketing opacity and the high transparency of the supernova in continuum opacity (Höflich et al. 1993) which causes the lack of flux in this region. However, the theoretical spectrum of Spyromilio et al. failed to fit the observations.

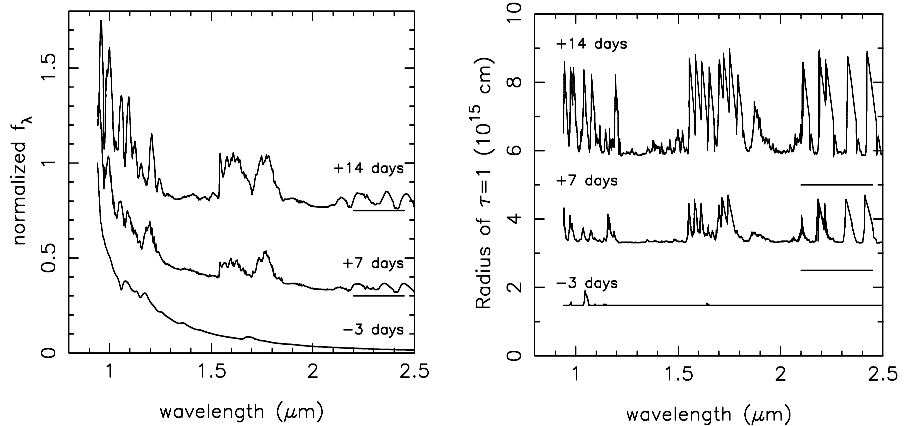


Figure 7. Evolution of the DD200 model spectrum and the radius of optical depth unity (times with respect to model V maximum).

Here, we want to discuss the formation of the IR-spectra more general. We want to show the unique potential of IR-spectroscopy of SNe Ia, and that the current generation of models allow for quantitative analyses. In Fig. 7, we give the evolution of the spectrum and of the radius at which of the optical depth is unity for DD200 are given with respect to model V maximum. They are -3, +7 and +14 days corresponding to about 15, 25, and 32 days after the explosion. The spectra have been normalized to the maximum flux in the displayed range and then a constant has been added for clarity of display. The levels of zero flux and radii are shown as straight lines in the red part of the spectra.

Three days before V maximum, the spectrum in Fig. 7 is relatively featureless with the exception of Mg II at $1.05 \mu\text{m}$. In DDs, it is produced as a natural consequence of burning and it is not due to He. Because Mg is produced mainly in the region of explosive carbon burning, the Doppler shift provides a unique tool to determine the transition zone from explosive carbon to oxygen burning. Early on, the IR-opacities are dominated by electron scattering. Later on, at wavelengths shorter than $\sim 1.2\text{-}\mu\text{m}$, the spectra are dominated by blends of Mg, Ca and iron group elements. With increasing time, the atmosphere becomes cooler. Once the electron scattering opacity decreases, a Type Ia supernova no longer has a well defined photosphere and the spectrum forming region varies with wavelength depending on the transition present at that frequency interval (Fig. 7). The features at about $1.5\text{--}1.7$ and $2.2\text{--}2.6\text{-}\mu\text{m}$ are primarily due to iron group elements of the second ionization stage. They appear in “emission” because they are formed at a larger radius and the source function is not scattering dominated, but governed by the redistribution of energy from higher frequencies (Höflich 1995).

Flux minima occur where the spectrum is formed at a small radius (Fig. 7). The broad holes in the opacity distribution may be used as a tool for analyzing the composition of the ejecta. The broad holes between $1.2\text{--}1.5$ and $1.9\text{--}2.1\text{-}\mu\text{m}$ correspond to a dispersion in velocity of $70,000$ and $30,000 \text{ km s}^{-1}$, far exceeding the dispersion of the expansion velocity of radioactive material in any super-

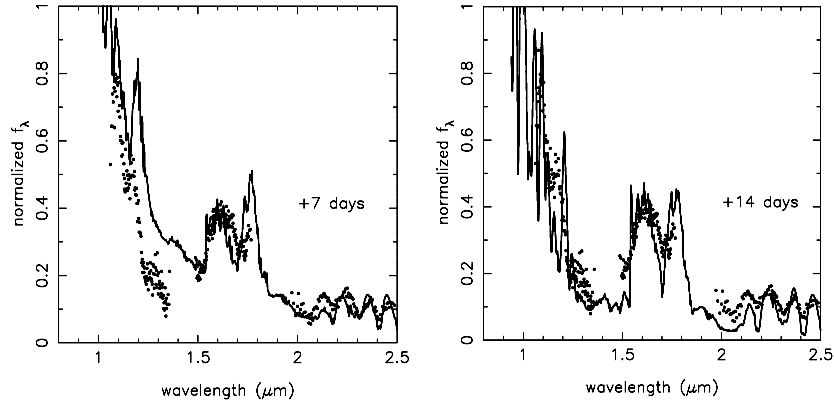


Figure 8. Synthetic spectra at +7 and +14d, and SN 1986G at +10d with respect to model and observed V maximum, respectively.

novae. Consequently, these gaps cannot be eliminated by velocity smearing and should in general be visible when the continuum opacity is low enough to expose them. The existence of the gaps provides the opportunity to probe very different layers of the ejecta at a given time. This makes the IR an important complement to the optical and the UV.

In Fig. 8, we compare the data from SN 1986G with the models. Note that SN 1986G is regarded to be a slightly subluminous, rapidly declining event compared to “normal” Type Ia supernovae. We neither tuned the models to provide a best fit nor reproduced the exact times of the observations. Instead, the goal of the comparison is to demonstrate that current generation of atmosphere codes is well suited to allow quantitative and that the IR is a valuable tool to analyze SNe Ia. For details, see Wheeler et al. (1997).

6. Distance Determinations & H_o

Based on our LCs, we have also determined the individual distances of the parent galaxies of the analyzed SNe Ia (sect. 5). Our method does not rely on secondary distance indicators and allows for a consistent treatment of interstellar reddening and the interstellar redshift. We find H_o to be $67 \pm 9 \text{ km/secMpc}$ within a 95 % confidence level (Fig. 9). This value agrees well with our previous analysis based on a subset of observations and models ($66 \pm 10 \text{ km Mpc}^{-1} \text{sec}^{-1}$, Müller & Höflich 1994). By using the brightness at maximum light alone (but including the individual reddening correction), our H_o decreases to $63 \text{ km Mpc}^{-1} \text{sec}^{-1}$.

Other determinations of H_o are based on independent, purely statistical methods and primary distance indicators. It may be encouraging that the result of different SN Ia based methods agree if SN Ia are not treated as standard candles. Tammann & Sandage (1995) found H_o of 54 ± 4 and 59 ± 4 using the B and V LC, respectively. Hamuy et al. (1995) get 65 ± 5 , Riess et al. (1995) give 67 ± 5 , and Fisher et al. (1995), Nugent et al. (1995b) and Branch et al. (1995) get a values of 60 ± 10 , 60 ± 12 and 58 ± 7 , respectively. Taking the excellent agreement between all methods, one may conclude that the question

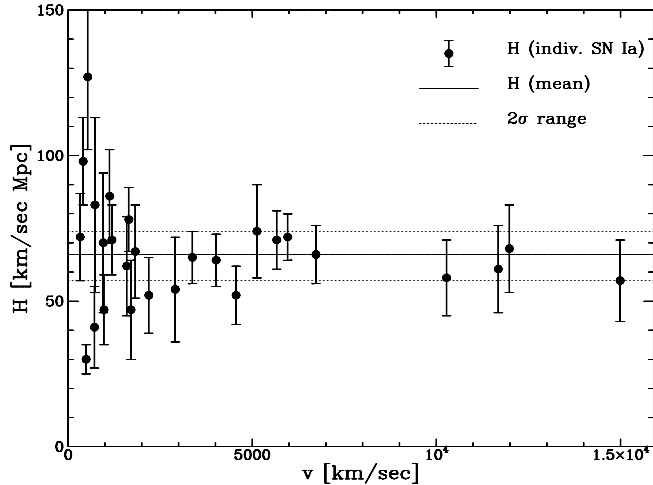


Figure 9. Hubble values H are shown based on individual distances based on fitting of the LCs and spectra (sect. 5 & HK96).

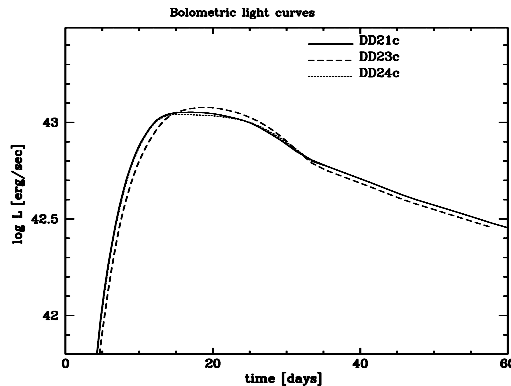
of H_0 has been settled at least within an 10 % error range. From our models, both the empirical relations between $M_V/dM(15)$ like-relations and the ansatz to deselect subluminous SNeIa seems to be justified, but we expect an individual dispersion of $\approx 20\%$ (Höfllich et al. 1996). Therefore more detailed analysis are needed to reduce the uncertainties beyond the current point.

7. Evolutionary Effects and Consequences for the Determination of Ω_M and Λ

Time evolution is expected to produce the following main effects: (a) a lower metallicity will decrease the time scale for stellar evolution of individual stars by about 20 % from Pop I to Pop II stars (Schaller et al. 1992) and, consequently, the progenitor population which contributes to the SNe Ia rate at any given time. The stellar radius also shrinks. This will influence the statistics of systems with mass overflow; (b) Evolutionary effects of the stellar population will change the mass function present at the time corresponding to a given redshift; (c) The initial metallicity Z will effect the nuclear burning during the explosion or, more precisely, the electron to nucleon fraction (sect. 3); (d) Systems with a shorter life time may dominate early on and, consequently, the typical C/O ratio of the central region of the WD is reduced; (e) In principle, a change of the metallicity may alter the R-M relation of a WD but this issue is not a major concern (Höfllich et al. 1997b); (f) The properties of the interstellar medium may change.

Before discussing the *possible (!)* implications for cosmology in more detail, we address the influence of changes in the initial composition on individual light curves and spectra, i.e. (c) and (d). The influence of the initial composition on light curves and spectra has been studied for the example of a set of delayed detonation models with DD21c being the reference model (Table 1). Because the time evolution of the composition is not well known and because we have not considered the entire variety of possible models, the values given below *do*

Figure 10. Comparison of bolometric LCs of the delayed detonation models DD21c, DD23c and DD24c with otherwise identical parameters but with different C/O ratios and metallicity relative to solar (C/O; R_Z) of (1;1), (2/3;1) and (1;0.3), respectively.



not (!) provide a basis for quantitative corrections of existing observations. The goal is to get a first order estimate of the size of the systematic effects to be expected, to demonstrate how evolutionary effects in a real data sample can be recognized and how one may be able to compensate.

7.1. Light Curves

Reducing the ratio C/O from 1/1 to 2/3 in the WD reduces the ^{56}Ni production and the kinetic energy in DD23c compared to DD21c. The smaller expansion due to the smaller E_{kin} causes a slower rise to maximum light by about 3 days. The smaller ^{56}Ni results in a steeper decline after maximum light because the photosphere recedes faster and the luminosity after about day 35 is smaller by about 10 % (Fig. 10). Both the bolometric and monochromatic light curves are effected by a similar amount because the energetics of the explosion changes. Overall, the change of the C/O ratio from 1/1 to 2/3 has a similar effect on the colors, light curve shape and the distribution of elements as a 10 % reduction in the transition density or central density in delayed detonations. However, for a given peak magnitude to tail ratio, a model produced by a reduced C/O ratio will be brighter than a one obtained by varying the transition density (Höfllich 1995). The rise time and the mean expansion rate provide a way to determine the C/O ratio and the transition density independently (compare Khokhlov et al., 1993, Höfllich 1995, HK96).

Changing the initial metallicity Z has very little influence on the bolometric light curve because the ^{56}Ni production and energy release vary by only 4 % if Z is varied between 0.1 and 10 times solar. In addition, diffusion time scales are mainly determined by deeper layers and, there, the electron capture during burning determines Y_e and not the initial composition (sect. 3).

7.2. Spectra at maximum light

Spectral changes due to the C/O ratio produce a variation in the pattern of the most abundant elements similar to a change in the transition density and the central density of the WD. Consequently, the variation of the spectra is similar. However, this degeneracy can be overcome if we combine the information from the LC with the expansion velocity measured by the line shifts.

More interesting is the influence of the initial metallicity because it influences the iron group elements even outside the region which underwent incom-

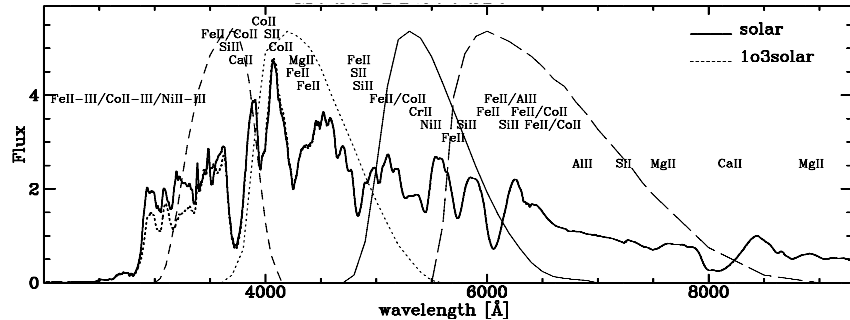


Figure 11. Comparison of synthetic NLTE spectra at maximum light for initial compositions of solar and 1/3 of solar, respectively. The standard Johnson filter functions for UBV, and R are also shown.

plete Si-burning during the explosion. As an example, the spectra of the delayed detonation models with solar and 1/3 solar metallicity are given in Fig. 11. At maximum light (≈ 17 days), the line forming region ($\tau \approx 0.1 \dots 1.$) extends between 1 and 2×10^{15} cm in the optical, corresponding to expansion velocities between 8000 and 16,000 km/sec (Fig.1). Consequently, the upper edge of the ^{56}Ni rich layers ($v \approx 12,000$ km/sec) become visible at maximum light and all but the far UV is formed in regions where at least partial burning to Si took place. The spectrum is scarcely effected by metallicity effects except for wavelengths below 4200 Å which are dominated by the layers with ^{54}Fe .

7.3. Implications for Cosmology

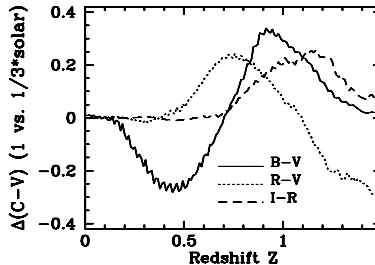
Systematic errors that must be taken into account in the use of SNe Ia to determine cosmological parameters include technical problems, changes of the environment with time, changes in the statistical properties of the SNe Ia, and changes in the physical properties of SNe Ia.

In the first class, we put corrections for redshift. If standard filter systems are used, they can be well calibrated to local standards but the k-correction is of some concern. This problem can be overcome if redshifted “standard” filters are used. Another technical problems may arise then from the fact that the transmission functions must be identical to those resulting from the redshift because no direct calibration can be applied by using a comparison star.

In the second class of problems an important example is that the properties of dust may change at high redshift. In the first place, the element abundances in the ISM can change. In addition, important donors of dust such as low mass stars during the red giant phase cannot contribute because their evolutionary time is comparable to or longer than the age of the universe at $z \approx 0.5$ to 1. Another problem related to the correction for extinction is that the extinction law to be applied depends on the redshift of the absorbing dust cloud (HK96).

In the third class of problems is the fact that the contribution of different progenitor types may change with redshift. For local supernovae, it is likely that a large variety of binary star properties (total mass of donor stars, separation, etc.) with very different evolutionary life times account for the variety of SNe Ia observed (Canal et al. 1997, Höflich et al. 1997a). Given this variety, we expect

Figure 12. Change of B-V, R-V, and I-R as a function of the redshift for DD21 when changing the initial abundance from solar to $1/3$ *solar.



a time evolution of the statistical properties of the progenitors because, early on, progenitors with a short life time will dominate the sample. Among other changes, more massive, shorter lifetime progenitors will have a lower C/O ratio in the center. Changes in the statistical properties are expected to increase with redshifts larger than 0.7 to 0.8 when the age of the univers becomes comparable or shorter than the suspected progenitor life times. Other evolutionary effects have already been mentioned: The ZAMS life time changes with metallicity, Roche lobe radii change with metallicity and the lower limit for accretion and steady burning of hydrogen on the surface of the WD changes by a factor of 2 for Pop I and Pop II stars, respectively (Nomoto et al., 1982).

Finally, the physical properties of a typical SNe Ia may change. If more massive stars contribute to the supernovae population, we expect a smaller mean C/O ratio. Changing the C/O ratio from $1/1$ to $2/3$ with otherwise identical parameters (see sect. 7.1), will result in a smaller ^{56}Ni production and, consequently, a lower bolometric luminosity at late times. On the other hand, the slower expansion causes less adiabatic cooling during early times and, thus, the luminosity at maximum light is larger. This implies that the peak to tail luminosity ratio changes. The consequences for the analysis by using light curve shapes or the postmaximum decline (e.g. δm_{15}) is evident. Quantitatively, for monochromatic light curves in our example, the difference in the peak to tail luminosity ratio is $\approx 0.2^m$. For techniques to determine the absolute peak luminosity by measuring either δm_{15} or LC shapes (e.g. Hamuy et al. 1996, Ries et al. 1995), this translates into a systematic error of $\approx 0.3^m$ in m_v . This systematic change in peak luminosity with redshift due to changing C/O ratios could mimic the effects of cosmology. Note that the transition density from deflagration to detonation may depend on the energy release during the deflagration phase and, hence the transition density could be a function of the C/O ratio, both effects could alter the LC.

The other physical effect on the SNe Ia themselves is the influence of the initial metallicity Z on the nuclear burning conditions during the explosion. This produces a change of the isotopic composition in the outer layers. A reduction of Z with redshift z is expected. Although small, the changes in the spectrum with metallicity have an important effect on the colors of SN at high red shifts where they are shifted into other bands (Fig. 12. For local SNe Ia, a change of the metallicity by a factor of 3 implies a variation in color of two to three hundredths of a magnitude. However, if the short wavelength part is shifted into the filter bands which are used, systematic effects of the order of several tenth of a magnitude can be expected. When using the color indices B-V, R-V and R-I, the systematic effects may be expected for $z \geq 0.2$, 0.5 and 0.7 , respectively.

Acknowledgments. Its a pleasure to thank all my collaborators and to thank G.A. Tammann and his (extended) group for the interesting discussions during my stay at the University of Basel.

References

- Abbot D.C., Lucy L.B. 1985, ApJ, 288, 679
Arnett, W.D. 1969, ApJS, 5, 180
Benz W., Thielemann F.K., Hills J.G. 1989, ApJ, 342, 986
Branch D., et al. 1996, Phys. Rep., in press
Branch D., Tammann G.A 1992, ARAA, 30, 359
Branch D. 1997, this volume
Canal R. 1995, Les Houches Lectures, eds. J. Audouze et al., Elsevier, in press
Castor, J.I. 1974, MNRAS, 169, 279
Collela P., Woodward P.R. 1984, J. Comp. Phys., 54, 174
Filippenko A.V. et al. 1992, AJ, 104, 1543
Hamuy M., Phillips M.M, Maza J., Suntzeff N.B., Schommer R.A., Aviles A. 1996, AJ, 112, 2438
Hansen, C.J., Wheeler, J.C. 1969, ApJS, 3, 464
Höflich, P., 1990, Habilitation thesis, U. of Munich, MPA 563
Höflich P. 1995, ApJ, 443, 89
Höflich P., Khokhlov A. 1996, ApJ, 457, 500
Höflich, P., Khokhlov, A., Müller, E. 1991, A&A, 248, L7
Höflich P., Khokhlov A., Müller E. 1992, A&A, 259, 243
Höflich, P., Müller, E.; Khokhlov, A. 1993, A&A, 268, 570
Höflich P., Khokhlov A., Wheeler J.C., Phillips M.M., Suntzeff N.B., Hamuy M., 1996, ApJ, 472, 81
Höflich P., Khokhlov A., Nomoto K., Thielmann F.K., Wheeler J.C. 1997a, eds. P. Ruiz-Lapuente, R. Canal, J. Isern, Nato ASI Series, Kluwer Academic Publisher, Vol. 486, 659
Höflich P., Wheeler J.C., Thielemann F.K 1997b, ApJ, in press
Iben, I.Jr., Tutukov, A.V. 1984, ApJS, 54, 335
Khokhlov A., Müller E., Höflich P. 1993, A&A, 270, 23
Khokhlov A. 1991ab, A&A, 245, & 114 & L25
Leibundgut, B. et al. 1995, ESO-Messenger 81, 19L
Leibundgut, B. et al. 1993, AJ, 105, 301
Karp, A.H., Lasher, G., Chan, K.L., Salpeter E.E. 1977, ApJ, 214, 161
Kurucz, R. 1993, Atomic Data for Opacity Calculations, Cambridge, Cfa
Livne E., Arnett D. 1995, ApJ, 452, 62
Meikle W.P.S. et al., 1996, MNRAS, 281, 263
Mihalas D., Kunasz R.B., Hummer D.G. 1975, ApJ, 202, 465
Mihalas D., Kunasz R.B., Hummer D.G. 1976a, ApJ, 206, 515

- Mihalas D., Kunasz R.B., Hummer D.G. 1976b, *ApJ*, 210, 419
- Müller E., Höflich P. 1994, *A&A*, 281, 51
- Nomoto K. 1980, *IAU-Sym.* 93, eds. D. Sugimoto, D.Q. Lamb & D. Schramm, Dordrecht, Reidel, 295
- Nomoto K., Yamaoka H., Shigeyama T., Iwamoto K., 1995, in: *Supernovae*, ed. R.A. McCray, Cambridge University Press, in press
- Nomoto K., Thielemann F.-K., Yokoi K. 1984, *ApJ*, 286, 644
- Nomoto K., Sugimoto D. 1977, *PASP*, 29, 765
- Nomoto K. 1982, *ApJ*, 253, 798
- Nomoto, K., Sugimoto, D., Neo, S. 1976, *ApJS*, 39, 137
- Norgaard-Nielsen H.U., Hansen L., Henning E.J., Salamanca A.A., Ellis R.S., Warrick, J.C., 1989, *Nature*, 339, 523
- Nugent P., Baron E., Hauschild P., Branch D. 1995a, *ApJ*, 441, 33
- Nugent P., et al. 1995b, *Phys. Rev. Let.*, 75, 394 & 1974E
- Olsson G.L., Auer L.H., Buchler J.R. 1986, *JQSRT*, 35, 431
- Pennypacker C. et al. 1991, *IAUC*, 5207
- Perlmutter C. et al. 1995, *ApJ Let*, 440, 95
- Perlmutter C. et al. 1997, *ApJ*, 483, 565
- Phillips M.M. et al. 1987, *PASP*, 90, 592
- Riess A.G., Press W.H., Kirshner R.P. 1995, *ApJ*, 438, 17
- Rybicki G.B., Press W.H. 1995, *Phys.Rev.Let.*, in press
- Saha A., Sandage A., Labhardt L., Tammann G.A., Machheotto F.D., Panagia N. 1997, *ApJ*, 486, 1
- Sandage A., Tammann G.A. 1993, *ApJ*, 415, 1
- Schaller G., Schaerer D., Meynet G., Maeder A. 1992, *A&A Suppl*, 96, 269
- Schmidt B.P, et al. 1996, *BAAS*, 189, 1089
- Sobolev V.V. 1957, *Sov. Astron.*, 1, 297
- Spyromilio J., Pinto P.A., Eastman R.G., 1994, *MNRAS*, 266, L17
- Thielemann F.-K. et al. 1994, in: *Supernovae*, Elsevier, Amsterdam, 629
- Thielemann F.-K., Arnould M., Truran J.W., 1987, *Advances in Nuclear Astrophysics*, E. Vangioni-Flam Editions frontières, Gif sur Yvette, 525
- Thielemann F.K., Nomoto K., Hashimoto M., 1996, *ApJ*, 460, 408
- Wells, L.A. et al. 1994, *AJ*, 108, 2233
- Wheeler J. C., Harkness R .P. 1990, *Rep. Prog. Phys.*, 53, 1467
- Wheeler J. C., Höflich P., Harkness R .P., Spyromilio J. 1997, *ApJ*, submitted
- Woosley S. E., Weaver T. A. 1994a, in: *Supernovae*, Elsevier, Amsterdam, p. 423
- Woosley S. E. & Weaver, T. A. 1994b, *ApJ*, 423, 371
- Woosley S. E., Weaver T.A., Taam R.E. 1980, in: *Type I Supernovae*, ed. J.C.Wheeler, Austin, U.Texas, 96

